PHYSICAL REVIEW B **94**, 045131 (2016)

Nature of charge density waves and superconductivity in $1T-\mathrm{TaSe}_{2-x}\mathrm{Te}_x$

Y. Liu (刘育),[1,*] D. F. Shao (邵定夫),[1,*] L. J. Li,[1] W. J. Lu,[1,†] X. D. Zhu,[2] P. Tong,[1] R. C. Xiao,[1] L. S. Ling,[2] C. Y. Xi,[2] L. Pi,[2]
H. F. Tian,[3] H. X. Yang,[3,‡] J. Q. Li,[3,4] W. H. Song,[1] X. B. Zhu,[1] and Y. P. Sun[2,1,5,§]

[1]*Key Laboratory of Materials Physics, Institute of Solid State Physics, Chinese Academy of Sciences,*
Hefei 230031, People's Republic of China
[2]*High Magnetic Field Laboratory, Chinese Academy of Sciences, Hefei 230031, People's Republic of China*
[3]*Beijing National Laboratory for Condensed Matter Physics, Institute of Physics, Chinese Academy of Sciences,*
Beijing 100190, People's Republic of China
[4]*Collaborative Innovation Center of Quantum Matter, Beijing 100190, People's Republic of China*
[5]*Collaborative Innovation Centre of Advanced Microstructures, Nanjing University, Nanjing 210093, People's Republic of China*

(Received 10 May 2016; revised manuscript received 12 July 2016; published 21 July 2016)

Transition-metal dichalcogenides (TMDs) MX_2 (M = Ti, Nb, Ta; X = S, Se, Te) exhibit a rich set of charge density wave (CDW) orders, which usually coexist and/or compete with superconductivity. The mechanisms of CDWs and superconductivity in TMDs are still under debate. Here we perform an investigation on a typical TMD system, $1T$-$\mathrm{TaSe}_{2-x}\mathrm{Te}_x$ ($0 \leqslant x \leqslant 2$). Doping-induced disordered distribution of Se/Te suppresses CDWs in $1T$-TaSe_2. A domelike superconducting phase with the maximum T_c^{onset} of 2.5 K was observed near CDWs. The superconducting volume is very small inside the CDW phase and becomes very large instantly when the CDW phase is fully suppressed. The observations can be understood based on the strong $\boldsymbol{q}$-dependent electron-phonon coupling-induced periodic-lattice-distortion (PLD) mechanism of CDWs. The volume variation of superconductivity implies the emergence of domain walls in the suppressing process of CDWs. Our concluded scenario makes a fundamental understanding about CDWs and related superconductivity in TMDs.

DOI: 10.1103/PhysRevB.94.045131

I. INTRODUCTION

Unconventional superconductivity refers to superconductivity that cannot be explained by the conventional electron-phonon coupling mechanism. Usually, unconventional superconductivity appears near the boundary of an ordered phase with broken translational or spin-rotation symmetry [1–3], so that it is thought to be tightly related to a (purely electronic) quantum critical point (QCP) [4,5]. Transition-metal dichalcogenides (TMDs) MX_2, where M = Ti, Nb, Ta, etc., and X = S, Se, Te, exhibit a rich set of Peierls-like charge density wave (CDW) orders [6]. Many typical TMDs show the coexistence and/or competition between conventional superconductivity and CDWs [7–16]. The resulting phase diagrams are very similar to those of unconventional superconductors, indicating that such superconductivity might be potentially due to a new kind of QCP unrelated to magnetic degrees of freedom [17–19]. However, QCP was recently found to be far away from superconductivity in $1T$-TiSe_2 under pressure [20].

A better understanding of the relation needs to clarify the origin of CDWs, which is a rather old but longstanding issue in condensed-matter physics [21–23]. The CDW and accompanying periodic lattice distortion (PLD) are usually explained by the Peierls picture [21–24]: Fermi-surface nesting, a pure electronic effect, drives the charge redistribution regardless of whether or not PLD subsequently happens. There is an opposite mechanism in which charge redistribution is driven by strong $\boldsymbol{q}$-dependent electron-phonon coupling-induced PLD, while Fermi-surface nesting only plays a minor role [24,25].

The typical system, $1T$-$\mathrm{Ta}X_2$ (X = S, Se, Te) [Figs. 1(a)–1(c)], is a good platform to investigate CDWs and superconductivity. Some reports have suggested that the Fermi-surface nesting leads to CDWs in the system [6,26–30], while some other investigations have supported the PLD mechanism [31,32]. Making a solid solution of different parent materials of the system and observing the variation of the CDW vector might help one to figure out the universal CDW mechanism. Moreover, the correlation effect opens a Mott gap of $5d$ band of Ta in commensurate (C) CDWs in $1T$-$\mathrm{Ta}X_2$ (X = S, Se) [15]. Suppression of CCDWs in $1T$-TaS_2 leads to a unique nearly commensurate (NC) CDW ground state, which is composed of a metallic incommensurate (IC) network and Mott-insulating CCDW domains [6]. Superconductivity emerges only in the percolated metallic interdomain area [8,12–14], which is clearly not related to the QCP. On the other hand, at low temperatures, $1T$-TaSe_2 exhibits CCDWs the same as $1T$-TaS_2 does [6]. However, no NCCDW phase has been found in $1T$-TaSe_2. Introducing superconductivity into $1T$-TaSe_2 and comparing it with the superconductivity in $1T$-TaS_2 might lead to a better understanding of the universal relation of CDWs and superconductivity in TMDs.

Previously, we found that the isovalent substitution in $1T$-$\mathrm{TaS}_{2-x}\mathrm{Se}_x$ ($0 \leqslant x \leqslant 2$) suppresses CCDWs and NCCDWs accompanied by superconductivity emergence in the middle doping area [14,15,33]. An ordered stacking of S/Ta/Se sandwiches is observed in $1T$-TaSSe [33]. In the present work, we prepared a series of $1T$-$\mathrm{TaSe}_{2-x}\mathrm{Te}_x$ ($0 \leqslant x \leqslant 2$) single crystals and obtained a phase diagram through the transport measurements. Different from the case in $1T$-$\mathrm{TaS}_{2-x}\mathrm{Se}_x$, we found that the doping induces Se/Te disorder in the system and suppresses CDWs when $0.5 < x < 1.5$. A domelike

---

[*] These authors contributed equally to this work.

[†] Corresponding author: wjlu@issp.ac.cn

[‡] Corresponding author: hxyang@iphy.ac.cn

[§] Corresponding author: ypsun@issp.ac.cn

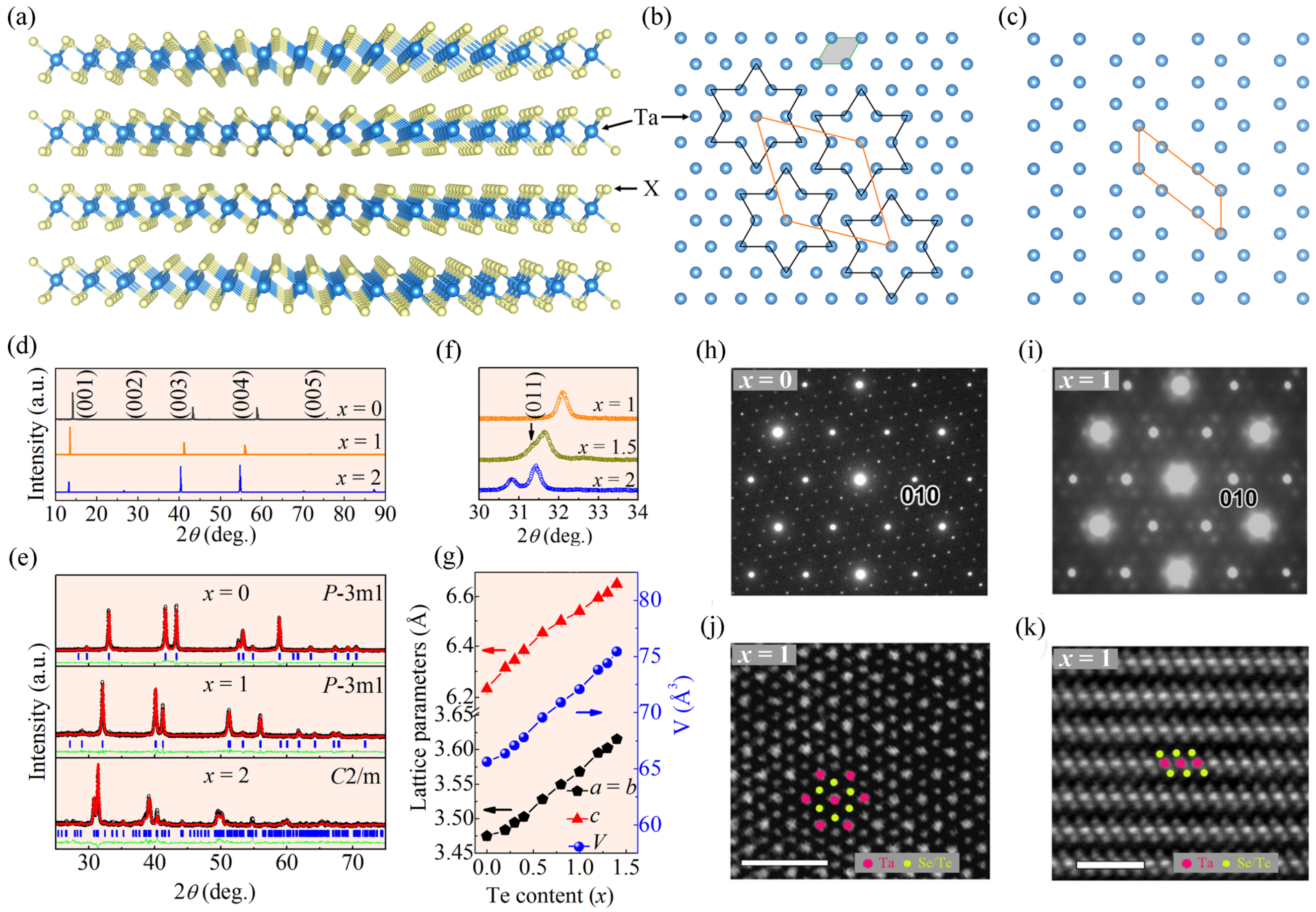

FIG. 1. (a) Crystal structure of ideal $1T$-TaX_2 (X = S, Se, Te). (b) Top view of Ta plane in $1T$-TaX_2 (X = S, Se). At low temperatures, Ta atoms displace to make “star of David” clusters, leading to 13.9° rotated $\sqrt{13}\times\sqrt{13}$ CCDWs with $\boldsymbol{q}_{\mathrm{CCDW}} = \frac{3}{13}\boldsymbol{a}^* + \frac{1}{13}\boldsymbol{b}^*$ [6]. (c) Top view of the Ta plane in TaTe$_2$. The monoclinic distorted-$1T$ structure of TaTe$_2$ can be seen as a 3×1 single-$\boldsymbol{q}$ CDW-type distorted structure of hypothetical $1T$-TaTe$_2$ [6,29,30]. (d) Single-crystal XRD patterns of $1T$-TaSe$_{2-x}$Te$_x$ for $x = 0$, 1, and 2, respectively. (e) Powder XRD patterns with Rietveld refinements of $1T$-TaSe$_{2-x}$Te$_x$ for $x = 0$, 1, and 2, respectively. (f) The enlargement of the (011) peaks of the powder XRD patterns of $1T$-TaSe$_{2-x}$Te$_x$ for $x = 1$, 1.5, and 2. (g) Evolution of lattice parameters (a, c) and cell volume (V) of $1T$-TaSe$_{2-x}$Te$_x$. Electron diffraction patterns of (h) $1T$-TaSe$_2$ and (i) $1T$-TaSeTe, taken along the [001] zone-axis direction. HAADF STEM images of $1T$-TaSeTe viewed from the (j) [001] and (k) [100] zone-axis direction. Scale bar, 1 nm.

superconductivity with maximum T_c^{onset} of 2.5 K was observed near CDW. The superconducting volume is very small inside the CDW phase and becomes very large instantly when the CDW phase is fully suppressed. Our observations can be clearly understood based on the PLD mechanism. The volume variation of superconductivity implies the emergence of domain walls when the CDW phase is suppressed.

II. EXPERIMENT AND CALCULATION DETAILS

Single crystals were grown by the chemical vapor transport (CVT) method with iodine as a transport agent. The high-purity elements Ta (4N), Se (4N), and Te (4N) were mixed in chemical stoichiometry, and heated at 900 °C for 4 days in an evacuated quartz tube. The harvested TaSe$_{2-x}$Te$_x$ powders and iodine (5 mg/cm^3) were then heated for 15 days in a two-zone furnace, where the temperatures of the source and growth zones were fixed at 950 °C and 850 °C, respectively.

The x-ray diffraction (XRD) patterns were obtained on a Philips X′pert PRO diffractometer with Cu K_α radiation ($\lambda = 1.5418$ Å). Structural refinements were performed by using the Rietveld method with the x′pert HIGHSCORE PLUS software. Electron diffraction and high-angle annular dark-field–scanning transmission electron microscopy (HAADF-STEM) experiments were performed in the JEOL ARM200F equipped with double aberration correctors and a cold field emission gun operated at 200 kV. For the STEM images, the convergence angle is 28 mrad and the collection angle of the HAADF detector is between 90 and 370 mrad. Under this condition, the spatial resolution is about 0.08 nm. The resistivity was measured by the standard four-probe ac technique using the Quantum Design Physical Property Measurement System (PPMS). Measurement of the temperature dependence of magnetic susceptibility and the isothermal hysteresis loop were carried out in the Quantum Design Magnetic Property Measurement System (MPMS) equipped with a ^{3}He cryostat.

The first-principles calculations based on density functional theory (DFT) were carried out using the QUANTUM ESPRESSO package [34] with ultrasoft pseudopotentials. The exchange-correlation interaction was treated with the local density approximation (LDA) according to Perdew and Zunger [35]. The energy cutoff for the plane-wave basis set was 35 Ry. Brillouin-zone sampling is performed on the Monkhorst-Pack (MP) mesh [36] of 32×32×8. The Vanderbilt-Marzari Fermi smearing method with a smearing parameter of $\sigma = 0.02$ Ry was used for the calculations of the total energy and electron charge density. Phonon dispersions were calculated using density functional perturbation theory (DFPT) [37] with an 8×8×4 mesh of $\boldsymbol{q}$ points. In order to investigate the distribution of CDW instability around the $\boldsymbol{q}_{\mathrm{CDW}}$, 16×16×1 $\boldsymbol{q}$ points were used. Denser 64×64×8 $\boldsymbol{k}$ points are used for electron-phonon coupling.

III. RESULTS AND DISCUSSION

A. Superconducting dome near CDWs

The x-ray diffraction (XRD) patterns of $1T$-TaSe$_{2-x}$Te$_x$ ($x = 0$, 1, and 2) single crystals are shown in Fig. 1(d), in which only (00l) reflections were observed, suggesting the c axis is perpendicular to the surface of the crystal. With increasing x, the diffraction peaks distinctly shift to lower angles, reflecting the crystal expansion induced by Te doping. Figure 1(e) shows the powder XRD patterns and the structural refinement results of Rietveld analysis for the selected samples with $x = 0$, 1, and 2. Figure 1(f) shows the enlargement of the (011) peak for $x = 1$, 1.5, and 2. The undistorted CdI$_2$-type $1T$ structure for $x = 1$ leads to a single (011) peak, while there are double peaks resulting from the monoclinic distorted-$1T$ structure for $x = 2$. As shown in Fig. 1(c), the (011) peak starts to split when $x = 1.5$, indicating the emergence of a distorted-$1T$ structure, i.e., the critical point between the $1T$-structure and monoclinic structure is close to $x = 1.5$. The evolution of the lattice parameters (a, c) and unit-cell volume (V) of $1T$-TaSe$_{2-x}$Te$_x$ is depicted in Fig. 1(g). Indeed, the values of a, c, and V monotonously increase with x, in accordance with the larger ion radius of Te than that of Se.

Figures 1(h) and 1(i) demonstrate two typical diffraction patterns taken along the [001] zone-axis direction of $1T$-TaSe$_2$ and $1T$-TaSeTe, respectively. The superstructure reflections corresponding to the commensurate phase with $\boldsymbol{q}_{\mathrm{CCDW}} = \frac{3}{13}\boldsymbol{a}^* + \frac{1}{13}\boldsymbol{b}^*$ can be clearly observed in Fig. 1(h), which is evidently different from the diffuse superlattice spots with the incommensurated in-plane $\boldsymbol{q}$ vector in $1T$-TaSeTe [Fig. 1(i)]. A similar result was previously reported by Luo *et al.* [38] and a possible chemical-origin, short-range Se/Te ordering was proposed. However, the detailed analysis based on the HAADF-STEM images seen from both [001] [Fig. 1(j)] and [100] [Fig. 1(k)] zone-axis directions suggests the disordered Se/Te distribution in the $1T$-TaSeTe, which is significantly different from the ordered S/Se distribution in $1T$-TaSSe [33].

Figures 2(a) and 2(b) show the temperature dependence of the in-plane resistivity ratio ($\rho/\rho_{250\,\mathrm{K}}$) of $1T$-TaSe$_{2-x}$Te$_x$ single crystals. The Te doping largely decreases the residual resistivity ratio (RRR $= \rho_{300\,\mathrm{K}}/\rho_{3\,\mathrm{K}}$). For $1T$-TaSe$_2$, RRR = 17.4. For $1T$-TaSeTe, RRR = 0.85, reflecting the substantial doping-induced disorder, which is corresponding to our HAADF-STEM observation. The signature of superconductivity emerges as $x \geqslant 0.3$, and finally disappears for $x \geqslant 1.3$, while the zero resistances are observed when $0.5 < x < 1.3$ [Fig. 2(a)]. The maximum of superconducting onset temperature (T_c^{onset}) of 2.5 K and the maximum of zero-resistance temperature (T_c^{zero}) of 1.6 K are found when the CDW phase is completely suppressed ($x = 0.6$). Figures 2(c) and 2(d) show the magnetic properties with both the zero-field-cooling (ZFC) and field-cooling (FC) modes of $1T$-TaSe$_{1.4}$Te$_{0.6}$ (optimal sample) and $1T$-TaSe$_{1.5}$Te$_{0.5}$ at $H = 10$ Oe with the magnetic field parallel to the c axis, respectively. The results indicate very small superconducting volume ($4\pi\chi = 2.7\times10^{-3}$ at 0.5 K in ZFC) in $1T$-TaSe$_{1.5}$Te$_{0.5}$ (in which the CDW phase still exists) and large superconducting volume ($4\pi\chi = 0.35$ at 0.5 K in ZFC) in $1T$-TaSe$_{1.4}$Te$_{0.6}$ (in which the CDW phase is just completely suppressed). The inset of Fig. 2(c) shows the magnetization hysteresis loop $M(H)$ obtained at $T = 0.5$ K, indicating it is a typical type-II superconductor. Figure 2(e) summarizes the overall phase diagram in $1T$-TaSe$_{2-x}$Te$_x$. The domelike superconducting phase is near the CDW phase, which is similar to that in $1T$-TaS$_{2-x}$Se$_x$[14]. In the phase diagram, the CDW phase is gradually suppressed by Te doping and disappears as $x > 0.5$, which is quite different from the situation in $1T$-TaS$_{2-x}$Se$_x$ [14]. With higher Te content $x > 1.5$, the crystal structure gradually distorts to a monoclinic one with the $C2/m$ space group, which could also be considered as a single-$\boldsymbol{q}$ CDW-type distortion [6,30].

B. Mechanisms of CDWs and superconductivity

The low-symmetry CDW structure is usually considered as the high-symmetry phase with distortion introduced by some instability. Since our prepared $1T$-TaSe$_{2-x}$Te$_x$ samples for $x < 1.5$ are all in the pure $1T$ phase according to the structure characterization, we performed the first-principles calculations using the $1T$ structure to explain our observation (Fig. 3). We first calculated the two end members of $1T$-TaSe$_2$ and hypothetical $1T$-TaTe$_2$, respectively. The fully optimized structural parameters, listed in Table I, are close to those from the previous LDA calculation [32]. The underestimation of lattice parameters is expected for LDA [32].

Previous research has shown that the phonon calculation is an effective method to simulate the CDW instability [29–32,39–41]. Figures 3(a) and 3(j) show the phonon dispersions of $1T$-TaSe$_2$ and $1T$-TaTe$_2$. For $1T$-TaSe$_2$, the calculation is in good agreement with the previous calculation by Ge *et al.* [32]. From Fig. 3(f), one can notice the calculated instability is just around the reported CCDW vector ($\boldsymbol{q}_{\mathrm{CCDW}} = \frac{3}{13}\boldsymbol{a}^* + \frac{1}{13}\boldsymbol{b}^*$) [26]. For $1T$-TaTe$_2$, the area of instability is centered near $\boldsymbol{q}_{\mathrm{CDW}} \approx \frac{1}{3}\boldsymbol{a}^*$ [Fig. 3(o)], which is corresponding to the reported (3×1) single-$\boldsymbol{q}$ CDW-type superlattice [29]. The high coincidence of the calculated and experimentally reported instabilities strongly proves the reliability and accuracy of the phonon calculation. Moreover, different from $1T$-TaSe$_2$, $1T$-TaTe$_2$ shows a much larger area of instability, which expands to the ΓK line [see Fig. 3(j)]. That might be the reason why $1T$-TaSe$_2$ only shows the small atomic displacement in the CDW phase, which can be suppressed at high temperatures,

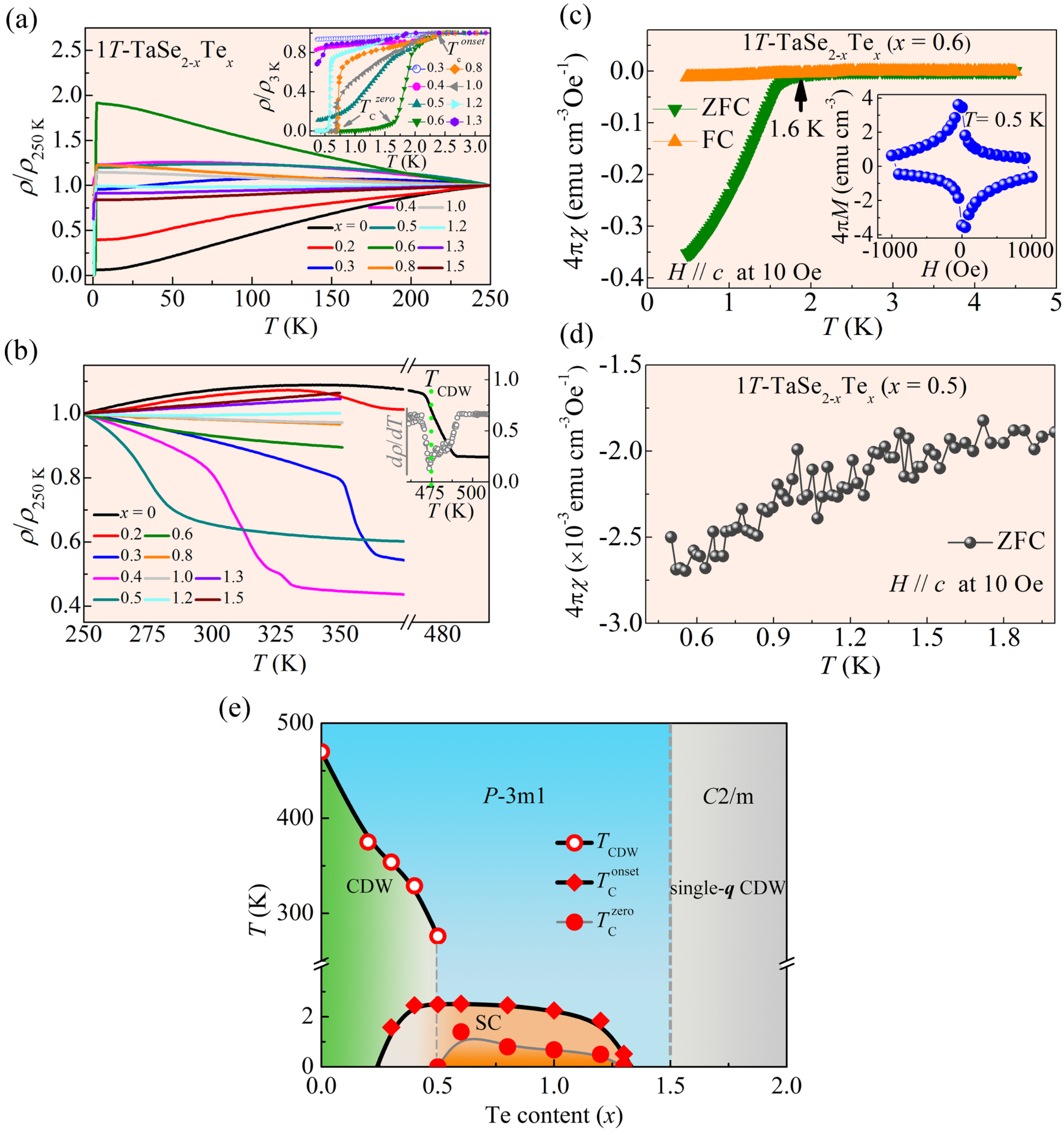

FIG. 2. Temperature dependence of in-plane resistivity ratio ($\rho/\rho_{250\,\mathrm{K}}$) of 1$T$-TaSe$_{2-x}Te_x$ (a) below $T = 250$ K and (b) above $T = 250$ K. Insets: the enlargement of superconducting transitions at low temperatures and the CCDW transition of 1T-TaSe$_2$ at high temperatures. Temperature dependence of magnetic susceptibility ($4\pi\chi$) with both the zero-field-cooling (ZFC) and field-cooling (FC) modes for (c) $x = 0.6$ and (d) $x = 0.5$. Inset: the magnetization hysteresis loop obtained at $T = 0.5$ K with magnetic field H paralleling the c axis. (e) Electronic phase diagram of 1T-TaSe$_{2-x}$Te$_x$ as a function of temperature and Te content.

while the single-$\boldsymbol{q}$ CDW-type distortion in TaTe$_2$ is very stable and the ideal-1T structure has never been observed.

Figures 3(b) and 3(k) show the band structures and Fermi surfaces of 1T-TaSe$_2$ and 1T-TaTe$_2$, respectively. For 1T-TaSe$_2$, early calculations show there is only one band crossing Fermi energy (E_F), which does not cross E_F in the vicinity of the Γ point [27,42]. Moreover, there is a gap (about 0.1 ∼ 0.2 eV) below the band crossing E_F [27,42]. However, the recent angle-resolved photoemission spectroscopy (ARPES) experiment clearly shows a hybridization of bands at Γ close to E_F, where small hole-type pockets are observed [43]. Obviously, our LDA calculations accurately simulated the band structure of 1T-TaSe$_2$ [Fig. 3(b)]. Three bands cross E_F: The lower two bands [colored in blue and orange in Fig. 3(b)]

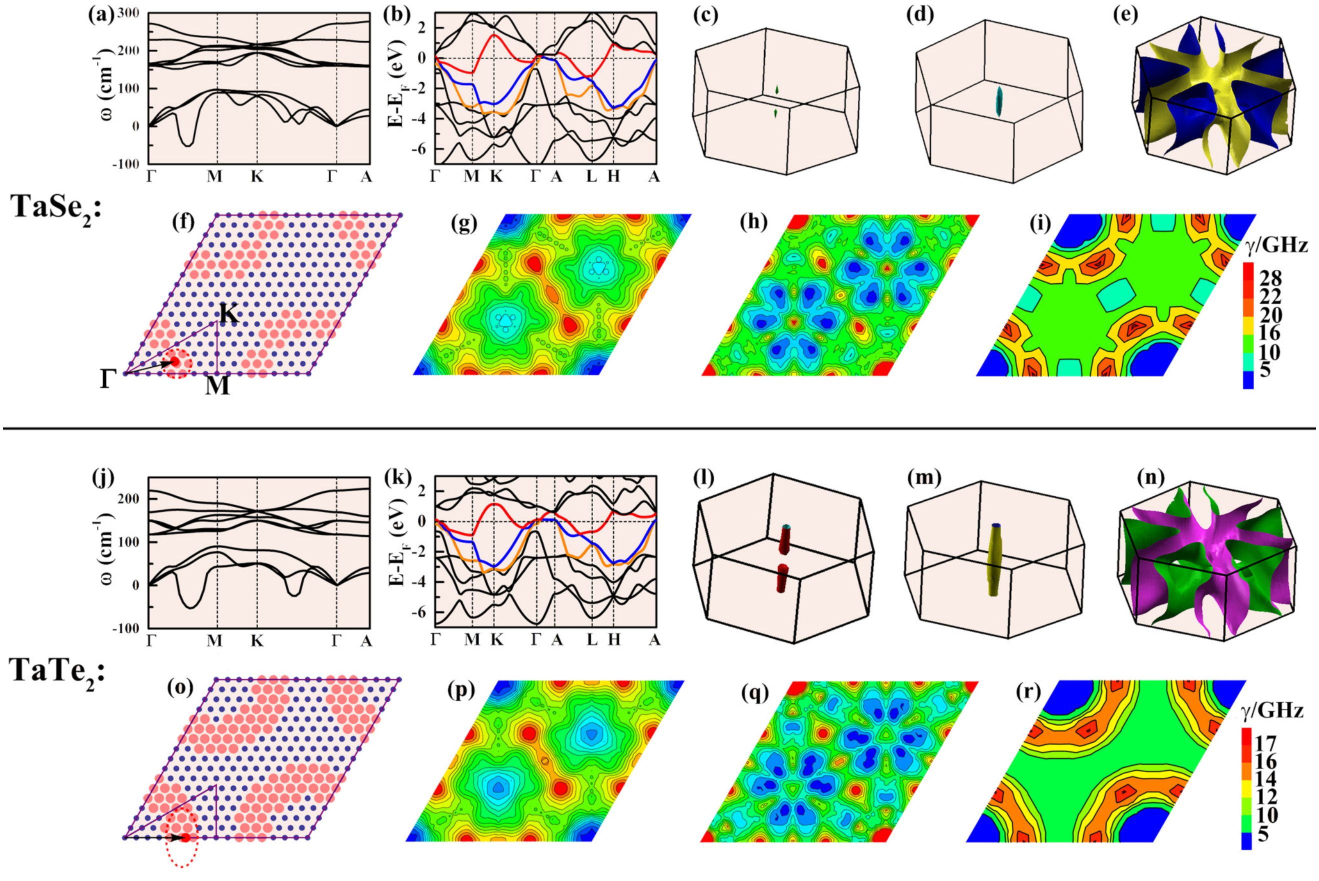

FIG. 3. The first-principles investigations on $1T$-TaSe$_2$ and $1T$-TaTe$_2$. The top panel shows the (a) phonon dispersions, (b) band dispersions, (c)–(e) Fermi surfaces, (f) distribution of instability in the $\boldsymbol{q}_z = 0$ plane, cross section of (g) real and (h) imaginary parts of the generated electron susceptibility with $\boldsymbol{q}_z = 0$, and (i) contour map of the phonon linewidth γ of the lowest phonon modes in the $\boldsymbol{q}_z = 0$ of $1T$-TaSe$_2$. (j)–(r) The bottom panel shows those of $1T$-TaTe$_2$. The bands crossing E_F are colored in (b) and (k). In (f) and (o), the pink solid circles denote the $\boldsymbol{q}$ points at which the frequency of the lowest mode is imaginary. The red solid circles and the black arrows in (f) and (o) denote the reported $\boldsymbol{q}_{\rm CCDW} = \frac{3}{13}\boldsymbol{a}^* + \frac{1}{13}\boldsymbol{b}^*$ and $\boldsymbol{q} \approx \frac{1}{3}\boldsymbol{a}^*$ for $1T$-TaSe$_2$ and $1T$-TaTe$_2$, respectively. The high-symmetry K points are shown in (f).

form small cylindrical hole-type pockets close to Γ [Figs. 3(c) and 3(d)]. The Fermi surface introduced from the higher band crossing $E_{\rm F}$ [colored in red in Fig. 3(b)] is shown in Fig. 3(e). For $1T$-TaTe$_2$, one can notice that the band structure and Fermi surfaces [Figs. 3(k)–3(n)] are highly similar to those of $1T$-TaSe$_2$.

The Fermi-surface nesting can be reflected in generated electron susceptibility [24]. The real part of the electron susceptibility is defined as

$$\chi'(\boldsymbol{q}) = \sum_{\boldsymbol{k}} \frac{f(\varepsilon_{\boldsymbol{k}}) - f(\varepsilon_{\boldsymbol{k}+\boldsymbol{q}})}{\varepsilon_{\boldsymbol{k}} - \varepsilon_{\boldsymbol{k}+\boldsymbol{q}}}, \tag{1}$$

where $f(\varepsilon_{\boldsymbol{k}})$ is the Fermi-Dirac function. The imaginary part is [24]

$$\chi''(\boldsymbol{q}) = \sum_{\boldsymbol{k}} \delta(\varepsilon_{\boldsymbol{k}} - \varepsilon_{\boldsymbol{F}})\delta(\varepsilon_{\boldsymbol{k}+\boldsymbol{q}} - \varepsilon_{\boldsymbol{F}}). \tag{2}$$

We used a mesh of approximately 40 000 $\boldsymbol{k}$ points in the full reciprocal unit cell to calculate the energy eigenvalues derived for the electron susceptibilities. Figures 3(g), 3(h), 3(p), and 3(q) show the cross section of the real part (χ') and imaginary part (χ'') of the electron susceptibility with $\boldsymbol{q}_z = 0$ for $1T$-TaSe$_2$ and $1T$-TaTe$_2$. We found that all of the maxima of χ' and χ'' locate between the Γ and M points. For $1T$-TaSe$_2$, both the maxima of χ' and χ'' locate at $\boldsymbol{q} \approx \frac{1}{3}\boldsymbol{a}^*$. The earlier calculation by Myron *et al.* [28] showed a peak of χ' at $\boldsymbol{q} \approx 0.28\boldsymbol{a}^*$, while the recent calculation by Yu *et al.* [44] reported a maximum of χ' at $\boldsymbol{q} \approx 0.295\boldsymbol{a}^*$. Clearly, the maxima of χ' and χ'' locate far away from $\boldsymbol{q}_{\rm CDW} = \frac{3}{13}\boldsymbol{a}^* + \frac{1}{13}\boldsymbol{b}^*$. Therefore, Fermi-surface nesting cannot account for the origin of CDWs in $1T$-TaSe$_2$.

We also calculated the electron-phonon coupling in the $\boldsymbol{q}_z = 0$ plane for $1T$-TaSe$_2$ and $1T$-TaTe$_2$. Figures 3(i) and 3(r) show the calculated phonon linewidth γ of the lowest

TABLE I. Structural parameters fully optimized by LDA for $1T$-TaSe$_2$, $1T$-TaTe$_2$, and $1T$-TaSeTe(O).

	a (Å)	c (Å)	$z_{\rm X}$
TaSe$_2$	3.406	6.086	$z_{\rm Se} = \pm 0.271$
TaTe$_2$	3.622	6.572	$z_{\rm Te} = \pm 0.274$
TaSeTe(O)	3.507	6.337	$z_{\rm Se} = 0.249$, $z_{\rm Te} = -0.296$

phonon modes in the $\boldsymbol{q}_z = 0$ plane. The phonon linewidth γ is defined by

$$\gamma_{\boldsymbol{q}\nu} = 2\pi\omega_{\boldsymbol{q}\nu} \sum_{ij} \int \frac{d^3k}{\Omega_{BZ}} |g_{\boldsymbol{q}\nu}(\boldsymbol{k},i,j)|^2 \times \delta(\varepsilon_{\boldsymbol{q},i} - \varepsilon_{\boldsymbol{F}})\delta(\varepsilon_{\boldsymbol{k}+\boldsymbol{q},j} - \varepsilon_{\boldsymbol{F}}), \tag{3}$$

where the electron-phonon coefficients $g_{\boldsymbol{q}\nu}(\boldsymbol{k},i,j)$ are defined as

$$g_{\boldsymbol{q}\nu}(\boldsymbol{k},i,j) = \left(\frac{\hbar}{2M\omega_{\boldsymbol{q}\nu}}\right)^{1/2} \langle\psi_{i,\boldsymbol{k}}|\frac{dV_{\mathrm{SCF}}}{d\hat{u}_{\boldsymbol{q}\nu}} \cdot \hat{\epsilon}_{\boldsymbol{q}\nu}|\psi_{j,\boldsymbol{k}+\boldsymbol{q}}\rangle, \tag{4}$$

where V_{SCF} is the Kohn-Sham potential, $\hat{u}$ is the atomic displacement, $\hat{\epsilon}$ is the phonon eigenvector, and ψ is the related wave function. According to this definition, γ, which reflects the electron-phonon coupling contribution, is a quantity that does not depend on the real or imaginary nature of the phonon frequency. Although the calculation with 16×16×1 $\boldsymbol{q}$ points is not enough to deduce the accurate vector with maximum γ, it can still qualitatively reflect the role of electron-phonon coupling. In the instability area, the γ of the lowest mode is hundreds of times larger than those of higher modes, proving the connection between electron-phonon coupling and CDWs. For 1*T*-TaSe$_2$, the biggest γ ($\sim$23.11 GHz) is found near the place where χ'' shows the maximum, which is understandable since Fermi-surface nesting can enhance γ according to Eqs. (3) and (4). The second largest γ ($\sim$22.18 GHz) is found in the place very near the reported $\boldsymbol{q}_{\mathrm{CDW}} = \frac{3}{13}\boldsymbol{a}^* + \frac{1}{13}\boldsymbol{b}^*$. Therefore, if we neglect the enhancement of nesting, one can find that the area of $\boldsymbol{q}$ points with large γ is centered at the reported $\boldsymbol{q}_{\mathrm{CDW}}$. For 1*T*-TaTe$_2$, the large γ area is strongly broadened and expands to Γ*K*, which is coinciding with the phonon instability area shown in Fig. 3. Meanwhile, χ' and χ'' show a small value in the place between Γ and *K*. Therefore, we can conclude that the $\boldsymbol{q}$-dependent electron-phonon coupling-induced PLD, instead of Fermi-surface nesting, is responsible for CDWs in 1*T*-TaSe$_{2-x}$Te$_x$.

In order to explain the suppression of CDWs upon Te doping, we calculated the simplest hypothetical sample 1*T*-TaSeTe with an ordered stacking of Se/Ta/Te, which is represented as 1*T*-TaSeTe(O). For comparison, we calculated the isostructural 1*T*-TaSSe(O), in which the ordered stacking of S/Ta/Se is experimentally demonstrated [33]. Both the phonon dispersions of 1*T*-TaSeTe(O) and 1*T*-TaSSe(O) show the CDW instability (Fig. 4), which means if the S/Se or Se/Te are orderly distributed, CDW could not be suppressed. Therefore, our observed suppression of CDW is due to the doping-induced disorder. From Table I, one can notice that the optimized z coordinates of X atoms in pristine 1*T*-TaX_2 (X = Se, Te) are about ±0.27. However, for 1*T*-TaSeTe(O), the z coordinates of X atoms change to $z_{\mathrm{Se}} = 0.249$ and $z_{\mathrm{Te}} = -0.296$, which indicates that the TaX_6 octahedra are largely distorted. When the Se and Te atoms are randomly mixed, random distortions of TaX_6 octahedra can be expected in reality, leading to the puckered Ta-Ta layers. This is not compatible with pure two-dimensional PLD. The above scenario can account for the fact that the disorder completely suppresses CDWs in the 1*T*-TaSe$_{2-x}$Te$_x$ system.

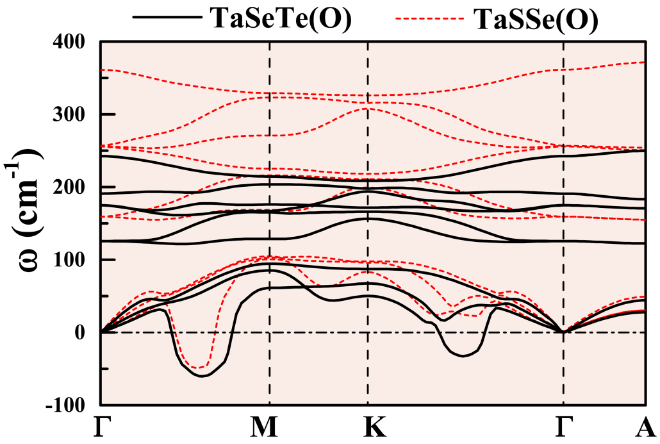

FIG. 4. Phonon dispersions of 1*T*-TaSeTe(O) and 1*T*-TaSSe(O).

We also try to understand the superconductivity near CDWs based on the PLD mechanism. The electron-phonon coupling strength for each mode ($\lambda_{\boldsymbol{q}\nu}$) is defined as

$$\lambda_{\boldsymbol{q}\nu} = \frac{\gamma_{\boldsymbol{q}\nu}}{\pi\hbar N(\varepsilon_{\boldsymbol{F}})\omega_{\boldsymbol{q}\nu}^2}. \tag{5}$$

An imaginary frequency ω of the phonon mode indicates the dynamical instability (in our cases, it indicates the CDW distortion). When the CDW phase is suppressed, the stabilizing of the 1*T* structure will make the imaginary frequency ω around $\boldsymbol{q}_{\mathrm{CDW}}$ become a small real value [31,32]. The large γ and small real ω in Eq. (5) can cause a large electron-phonon coupling constant, leading to the superconductivity. However, it is still hard to understand the part of the superconducting phase locating inside the CDW area of the phase diagram.

C. Universal schematic phase diagrams

1*T*-TaS$_2$ and 1*T*-TaSe$_2$ have the same CCDW ground state, but the CDW transitions in them are different. For 1*T*-TaSe$_2$, just like most TMDs, ICCDW seems to emerge only when CCDW is fully suppressed. On the contrary, in 1*T*-TaS$_2$, when CCDW is suppressed, domain walls instantly emerge and cut the previous long-range CCDW into CCDW domains, leading to the NCCDW state. The CCDW domains gradually shrink, while ICCDW grows in interdomain areas. When the CCDW domains disappear, the system transforms to the ICCDW state. That characteristic makes 1*T*-TaS$_2$ very unique among the TMDs with CDWs in a long time [6].

In CCDW states of 1*T*-TaS$_2$ and 1*T*-TaSe$_2$, the 5*d* band of Ta opens a Mott gap, which should prohibit the superconductivity inside the CCDW phase. In the NCCDW state of 1*T*-TaS$_2$, the CCDW domains remain Mott insulating, and superconductivity can only emerge in the metallic interdomain area [8]. In our present 1*T*-TaSe$_{2-x}$Te$_x$, considering the observed very small superconducting volume inside the CDW phase, one can expect that the domain walls emerge when the CDW phase is suppressed, just like the case demonstrated in 1*T*-TiSe$_2$ under pressure [20]. Very recently, the coexistence of CCDW and ICCDW phases was observed during the photoinduced suppression of CDW in 1*T*-TaSe$_2$ [45], which supports our concluded scenario. Since domelike superconductivity is usually found in TMDs with CDWs, the domain walls should

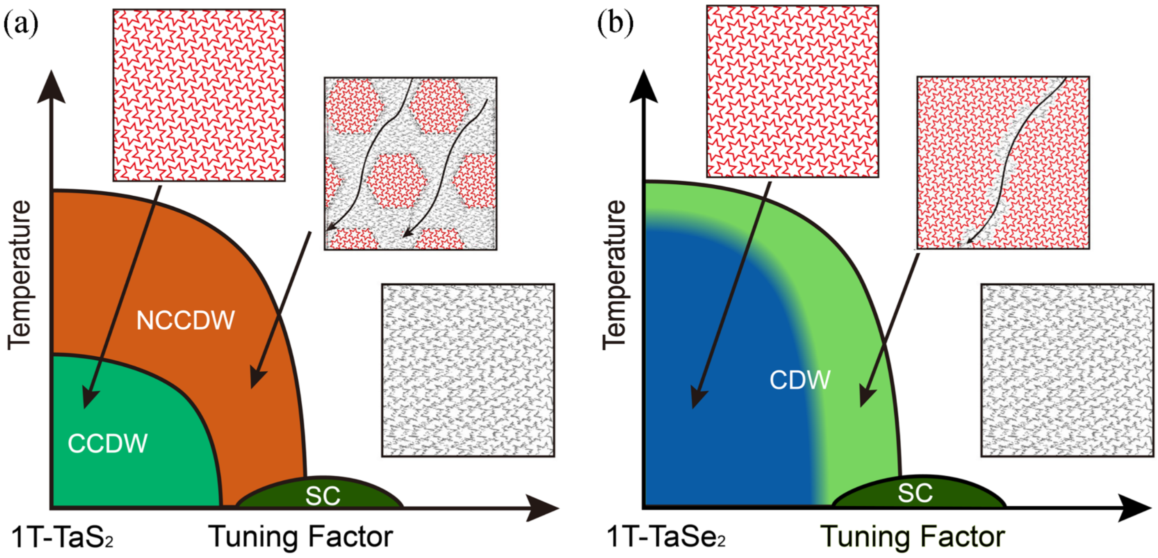

FIG. 5. The schematic tuning phase diagrams of (a) 1*T*-TaS_2 and (b) 1*T*-$TaSe_2$.

be universal, although they are hard to reflect in the routine measurements.

Thus we can illustrate the universal natures of CDWs and related superconductivity in some TMDs such as 1*T*-TaS_2, 1*T*-$TaSe_2$, and 1*T*-$TiSe_2$. At $\boldsymbol{q}_{\text{CDW}}$, the strong electron-phonon coupling largely softens the phonon modes. Below T_{CDW}, the phonon energy at $\boldsymbol{q}_{\text{CDW}}$ becomes imaginary, meaning there is a new lattice structure. Since the CDW phase originates from the strong $\boldsymbol{q}$-dependent electron-phonon coupling-induced PLD instead of the Fermi-surface nesting, the CDW gap does not need to be opened exactly at E_{F} when the CDW transition happens. Therefore, there is no reason to have a metal-insulator transition associated with the CDW transition [46].

We drew the schematic phase diagrams to show the tuning process of CDWs in those systems (Fig. 5). The tuning factor such as doping or pressure can harden the phonon mode at $\boldsymbol{q}_{\text{CDW}}$. When the phonon energy at $\boldsymbol{q}_{\text{CDW}}$ becomes real, the CDW phase is suppressed. The suppression probably first happens in a small area, leading to the emergence of domain walls. In 1*T*-TaS_2, the interdomain areas grow and the domains shrink upon tuning. When the domains disappear, the CDW is fully suppressed [Fig. 5(a)]. For 1*T*-$TaSe_2$ and 1*T*-$TiSe_2$, in CDW order, the domain walls are strongly pinned. In that case, the volumes of filamentlike interdomain areas are very small, so that the routine phase diagram [Fig. 2(e)] based on the transport measurements cannot reflect the situation. A more accurate phase diagram obtained by some measurements with high resolution should follow the schematic diagram presented in Fig. 5(b). The mechanism of different pinning of domain walls in 1*T*-$TaSe_2$ and other systems needs to be further investigated.

The superconductivity near CDWs is not due to QCP, but to the emergence of domain walls. In the interdomain areas, as the CDW phase is just suppressed, the phonon frequency at $\boldsymbol{q}_{\text{CDW}}$ has a small real value, leading to a large total electron-phonon coupling constant. Once the interdomain areas percolated, superconductivity emerges (Fig. 5). When the system is far away from CDWs, the phonon frequency at $\boldsymbol{q}_{\text{CDW}}$ become larger, and thus the total electron-phonon coupling constant decreases. Therefore, a domelike superconducting phase can be obtained.

IV. CONCLUSION

In conclusion, we prepared a series of 1*T*-$TaSe_{2-x}Te_x$ ($0 \leqslant x \leqslant 2$) single crystals and summarized an overall electronic phase diagram through the transport measurements. The CDW phase in 1*T*-$TaSe_{2-x}Te_x$ ($0 \leqslant x \leqslant 2$) is gradually suppressed by Te doping-induced Se/Te disorder and finally disappears when $x > 0.5$. A domelike superconducting phase with the maximum $T_{\text{c}}^{\text{onset}}$ of 2.5 K is observed near CDWs. The superconducting volume is very small inside the CDW phase and becomes very large instantly when the CDW phase is fully suppressed. Based on the first-principles calculations, we found that the origin of CDWs in the system should be the strong $\boldsymbol{q}$-dependent electron-phonon coupling-induced PLD, instead of Fermi-surface nesting. In this framework, the nature of CDWs and superconductivity can be well understood. The volume variation of superconductivity implies the emergence of domain walls in the suppressing process of CDWs. Our concluded scenario makes a fundamental understanding about CDWs and related superconductivity in TMDs.

ACKNOWLEDGMENTS

This work was supported by the National Key Research and Development Program under Contract No. 2016YFA0300404, the National Natural Science Foundation of China under Contracts No. 11404342, No. 11274311, and No. 11190022, the National Basic Research Program of China under Contract No. 2015CB921300, the Joint Funds of the National Natural Science Foundation of China and the Chinese Academy of Sciences' Large-scale Scientific Facility (Grant No. U1232139), Anhui Provincial Natural Science Foundation under Contract No. 1408085MA11, and the Director's Fund under Contract No. YZJJ201311 of Hefei Institutes of Physical Science, Chinese Academy of Sciences.

[1] N. D. Mathur, F. M. Grosche, S. R. Julian, I. R. Walker, D. M. Freye, R. K. W. Haselwimmer, and G. G. Lonzarich, Nature (London) **394**, 39 (1998).
[2] J. M. Tranquada, B. J. Sternlieb, J. D. Axe, Y. Nakamura, and S. Uchida, Nature (London) **375**, 561 (1995).
[3] P. C. Canfield and S. L. Budko, Annu. Rev. Condens. Matter Phys. **1**, 27 (2010).
[4] V. A. Sidorov, M. Nicklas, P. G. Pagliuso, J. L. Sarrao, Y. Bang, A. V. Balatsky, and J. D. Thompson, Phys. Rev. Lett. **89**, 157004 (2002).
[5] J. L. Tallon *et al.*, Phys. Stat. Sol. B **215**, 531 (1999).
[6] J. A. Wilson, F. J. Di Salvo, and S. Mahajan, Adv. Phys. **24**, 117 (1975).
[7] Y. J. Yu, F. Y. Yang, X. F. Lu, Y. J. Yan, Y.-H. Cho, L. G. Ma, X. H. Niu, S. Kim, Y.-W. Son, D. L. Feng, S. Y. Li, S.-W. Cheong, X. H. Chen, and Y. B. Zhang, Nat. Nanotechnol. **10**, 270 (2015).
[8] B. Sipos, A. F. Kusmartseva, A. Akrap, H. Berger, L. Forró, and E. Tutiš, Nat. Mater. **7**, 960 (2008).
[9] E. Morosan, H. W. Zandbergen, B. S. Dennis, J. W. G. Bos, Y. Onose, T. Klimczuk, A. P. Ramirez, N. P. Ong, and R. J. Cava, Nat. Phys. **2**, 544 (2006).
[10] E. Morosan, K. E. Wagner, L. L. Zhao, Y. Hor, A. J. Williams, J. Tao, Y. Zhu, and R. J. Cava, Phys. Rev. B **81**, 094524 (2010).
[11] K. E. Wagner, E. Morosan, Y. S. Hor, J. Tao, Y. Zhu, T. Sanders, T. M. McQueen, H. W. Zandbergen, A. J. Williams, D. V. West, and R. J. Cava, Phys. Rev. B **78**, 104520 (2008).
[12] L. J. Li, W. L. Lu, X. D. Zhu, L. S. Ling, Z. Qu, and Y. P. Sun, Europhys. Lett. **97**, 67005 (2012).
[13] R. Ang, Y. Tanaka, E. Ieki, K. Nakayama, T. Sato, L. J. Li, W. J. Lu, Y. P. Sun, and T. Takahashi, Phys. Rev. Lett. **109**, 176403 (2012).
[14] Y. Liu, R. Ang, W. J. Lu, W. H. Song, L. J. Li, and Y. P. Sun, Appl. Phys. Lett. **102**, 192602 (2013).
[15] R. Ang, Y. Miyata, E. Ieki, K. Nakayama, T. Sato, Y. Liu, W. J. Lu, Y. P. Sun, and T. Takahashi, Phys. Rev. B **88**, 115145 (2013).
[16] Y. Liu, L. J. Li, W. J. Lu, R. Ang, X. Z. Liu, and Y. P. Sun, J. Appl. Phys. **115**, 043915 (2014).
[17] A. F. Kusmartseva, B. Sipos, H. Berger, L. Forró, and E. Tutiš, Phys. Rev. Lett. **103**, 236401 (2009).
[18] S. Y. Li, G. Wu, X. H. Chen, and L. Taillefer, Phys. Rev. Lett. **99**, 107001 (2007).
[19] H. Barath, M. Kim, J. F. Karpus, S. L. Cooper, P. Abbamonte, E. Fradkin, E. Morosan, and R. J. Cava, Phys. Rev. Lett. **100**, 106402 (2008).
[20] Y. I. Joe, X. M. Chen, P. Ghaemi, K. D. Finkelstein, G. A. de la Peña, Y. Gan, J. C. T. Lee, S. Yuan, J. Geck, G. J. MacDougall, T. C. Chiang, S. L. Cooper, E. Fradkin, and P. Abbamonte, Nat. Phys. **10**, 421 (2014).
[21] R. E. Peierls, *Quantum Theory of Solids* (Clarendon, Oxford, 1955).
[22] R. E. Peierls, *More Surprises in Theoretical Physics* (Princeton University Press, Princeton, NJ, 1991).
[23] H. Fröhlich, Proc. R. Soc. A **223**, 296 (1954).
[24] M. D. Johannes and I. I. Mazin, Phys. Rev. B **77**, 165135 (2008).
[25] S. K. Chan and V. Heine, J. Phys. F: Metal Phys. **3**, 795 (1973).
[26] S. Tanda, T. Sambongi, T. Tani, and S. Tanaka, J. Phys. Soc. Jpn. **53**, 476 (1984).
[27] H. W. Myron and A. J. Freeman, Phys. Rev. B **11**, 2735 (1975).
[28] H. W. Myron, J. Rath, and A. J. Freeman, Phys. Rev. B **15**, 885 (1977).
[29] C. Battaglia, H. Cercellier, F. Clerc, L. Despont, M. G. Garnier, C. Koitzsch, P. Aebi, H. Berger, L. Forró, and C. Ambrosch-Draxl, Phys. Rev. B **72**, 195114 (2005).
[30] S. Sharma, L. Nordstrom, and B. Johansson, Phys. Rev. B **66**, 195101 (2002).
[31] A. Y. Liu, Phys. Rev. B **79**, 220515(R) (2009).
[32] Y. Ge and A. Y. Liu, Phys. Rev. B **82**, 155133 (2010).
[33] R. Ang, Z. C. Wang, C. L. Chen, J. Tang, N. Liu, Y. Liu, W. J. Lu, Y. P. Sun, T. Mori, and Y. Ikuhara, Nat. Commun. **6**, 6091 (2015).
[34] P. Giannozzi, S. Baroni, N. Bonini, M. Calandra, R. Car, C. Cavazzoni, D. Ceresoli, G. L. Chiarotti, M. Cococcioni, I. Dabo, A. D. Corso, S. de Gironcoli, S. Fabris. G. Fratesi, R. Gebauer, U. Gerstmann, C. Gougoussis, A. Kokalj, M. Lazzeri, L. M.-Samos, N. Marzari, F. Mauri, R. Mazzarello, S. Paolini, A. Pasquarello, L. Paulatto, C. Sbraccia, S. Scandolo, G. Sclauzero, A. P. Seitsonen, A. Smogunov, P. Umari, and R. M. Wentzcovitch, J. Phys.: Condens. Matter **21**, 395502 (2009).
[35] J. P. Perdew and A. Zunger, Phys. Rev. B **23**, 5048 (1981).
[36] H. J. Monkhorst and J. D. Pack, Phys. Rev. B **13**, 5188 (1976).
[37] S. Baroni, S. de Gironcoli, A. D. Corso, and P. Giannozi, Rev. Mod. Phys. **73**, 515 (2001).
[38] H. X. Luo, W. W. Xie, J. Tao, H. Inoue, A. Gyenis, J. W. Krizan, A. Yazdani, Y. M. Zhu, and R. J. Cava, Proc. Natl. Acad. Sci. USA **112**, E1174 (2015).
[39] M. D. Johannes, I. I. Mazin, and C. A. Howells, Phys. Rev. B **73**, 205102 (2006).
[40] Y. Ge and A. Y. Liu, Phys. Rev. B **86**, 104101 (2012).
[41] M. Calandra and F. Mauri, Phys. Rev. Lett. **106**, 196406 (2011).
[42] A. M. Woolley and G. Wexler, J. Phys. C: Solid State Phys. **10**, 2601 (1977).
[43] M. Bovet, D. Popović, F. Clerc, C. Koitzsch, U. Probst, E. Bucher, H. Berger, D. Naumović, and P. Aebi, Phys. Rev. B **69**, 125117 (2004).
[44] X. L. Yu, D. Y. Liu, T. Jia, H. Q. Lin, and L. J. Zou, arXiv:1407.1407.
[45] S. S. Sun, L. L. Wei, Z. W. Li, G. L. Cao, Y. Liu, W. J. Lu, Y. P. Sun, H. F. Tian, H. X. Yang, and J. Q. Li, Phys. Rev. B **92**, 224303 (2015).
[46] X. T. Zhu, Y. W. Cao, J. D. Zhang, E. W. Plummer, and J. D. Guo, Proc. Natl. Acad. Sci. USA **112**, 2367 (2015).